THE EFFECT OF NON-EQUILIBRIUM BOUNDARY LAYERS ON COMPRESSOR PERFORMANCE

Andrew P.S. Wheeler*
Whittle Laboratory
Department of Engineering
Cambridge University
Cambridge, UK
Email: aw329@cam.ac.uk

Anthony M. J. Dickens
Whittle Laboratory
Department of Engineering
Cambridge University
Cambridge, UK

Robert J. Miller
Whittle Laboratory
Department of Engineering
Cambridge University
Cambridge, UK

ABSTRACT

The paper investigates the effect of non-equilibrium behaviour of boundary layers on the profile loss of a compressor. The investigation is undertaken using both high fidelity simulations of a mid-height section of a compressor blade and a reduced order model, MISES. The solutions are validated using experimental measurements made in the embedded stage of a multistage low speed compressor. The paper shows that up to 35% *of the suction surface boundary layer of the compressor blade exhibits non-equilibrium behaviour. The size of this region reduces as the Reynolds number is increased. The non-equilibrium behaviour was found to reduce profile loss in cases of attached transition and raise loss where transition occurs through separation.*

INTRODUCTION

In an aero-engine compressor approximately 40% of the losses are caused by profile loss [1]. The profile loss is largely determined by the boundary layer development over the blade surface, which creates entropy through viscous shear work. Denton (1993) [2] shows that for a boundary layer, the entropy production rate per unit surface area is

$$\dot{S_a} = c_d \frac{\rho {U_e}^3}{T}, \tag{1}$$

where the dissipation coefficient c_d is a function of the Reynolds number and boundary layer state; typically the dissipation coefficient for laminar boundary layers can be between $2-5$ times lower than for a turbulent one. Therefore, maintaining laminar flow over a significant portion of the blade surface can lead to large reductions in loss. It is largely for this reason and the need to avoid boundary-layer separation, that there have been many studies of boundary-layer transition in compressors blade-rows (see [3–6]).

The view promoted by equation 1 is that the dissipation coefficient c_d is to a large extent only dependent on the boundary layer state, and that loss is determined by the amounts of laminar and turbulent wetted area and loading distribution. Underlying this is the impression that boundary layers exist in two equilibrium states, either laminar or turbulent. A turbulent boundary layer in equilibrium is a boundary layer where the shape of the boundary layer does not vary significantly in the streamwise direction [7]. In reality turbulent boundary layers on compressor blades can behave in a significantly non-equilibrium way. Examples of this include attached boundary layers undergoing transition and reattaching boundary layers. The central aim of this paper is to determine the effect that these non-equilibrium processes can have on profile loss. This paper shows that even after transition is complete, the boundary layer continues to be in a non-equilibrium state for up to 35% of the suction surface.

In order to illustrate this, Figure 1 shows the suction surface boundary layer states found in the compressor blade studied in this paper. Below these are also shown the variation in turbulence production and dissipation coefficient. Here we discuss only the suction surface, since this is of most importance to loss. Figure 1 has been put together using data from simulations discussed later in the paper.

Across the transition region turbulence production rises, reaches a peak where the flow becomes fully turbulent and then falls back to an equilibrium level over the aft portion of the boundary layer. The rise in turbulence production gives rise to a large increase in dissipation coefficient across the transition region.

Also shown are the dissipation coefficient for laminar and equilibrium turbulent boundary layers as determined by correlations using the local shape factor H and momentum thickness Reynolds number Re_θ computed from the simulations [8]. The equilibrium dissipation coefficient which is initially very high at transition, rapidly drops to the normal level for attached turbulent boundary layers ($c_d = 0.002$). There is an appreciable difference in the actual dissipation coefficient and the equilibrium values (around 40%) due to the lag between production and dissipation of turbulence. In this paper we show that this is important, because the lag means that the peak dissipation coefficient is re-

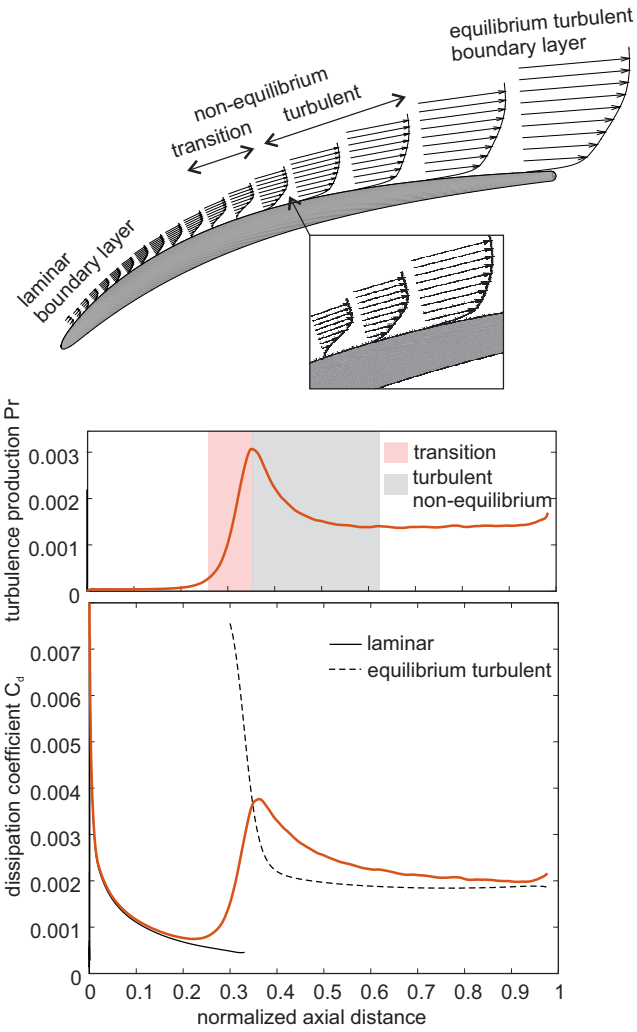

FIGURE 1. Schematic of boundary layer states on a compressor blade suction surface (top). Middle and lower plots show the variation in turbulence production and dissipation coefficient determined from high fidelity CFD ($Re = 340k$).

duced compared to the peak equilibrium level, which tends to reduce overall losses.

In this paper we aim to answer three questions:

1. What percentage of the turbulent boundary layer behaves in a non-equilibrium way?
2. What is the physical mechanism responsible?
3. What is the impact of non-equilibrium behaviour on profile loss?

These questions are answered in this paper using a combination of high fidelity simulations and reduced-order modelling.

COMPUTATIONAL DETAILS

In the first part of the paper we describe the high-order computational method used. We then describe implicit large eddy and direct numerical simulations of a high-pressure compressor stator passage with freestream turbulence. The simulations are first compared with experimental measurements within a 3-stage

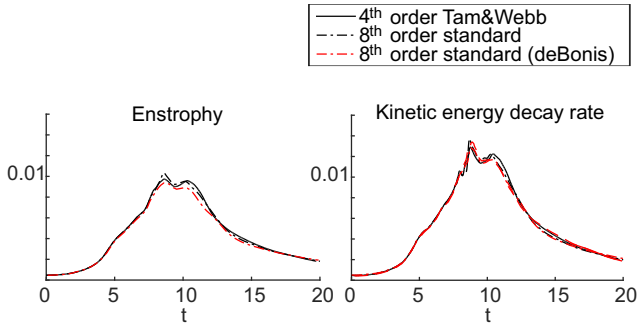

FIGURE 2. Comparison of enstrophy and kinetic energy decay rate against time from the the Taylor-Green vortex case results of de Bonis (red) with *3DNS* code using 4^{th} order Tamm and Webb ($-$) and 8^{th} order ($-\cdot-$) discretizations with 128^3 mesh points

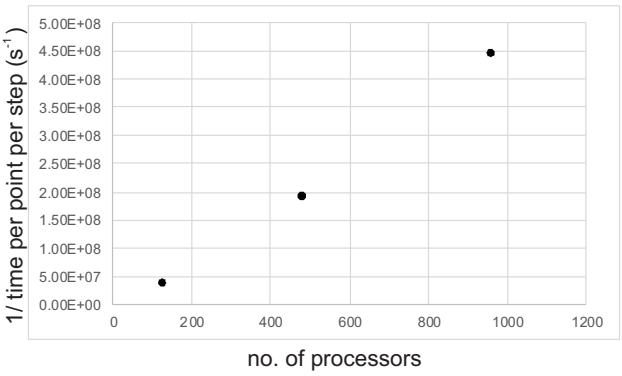

FIGURE 3. Code performance on the *Re3E5* case (see table 1)

TABLE 1. Test cases for Reynolds number study

Test-case label	Mesh (no. points)	*Re*	*Tu*	Span/C_{ax}
Re4E5F	Fine (127M)	408k	3.5%	0.1
Re3E5	Datum (63M)	340k	3.5%	0.1
Re2E5	Datum (63M)	220k	3.5%	0.1
Re1E5	Datum (63M)	110k	3.5%	0.1
Re1E5W	Datum (63M)	110k	3.5%	0.2

compressor in order to ensure that representative free-stream turbulence is prescribed and that the predicted total pressure loss matches experimental data.

Solver details

A new high-order code *'3DNS'* is used for this investigation. *3DNS* is a compressible finite-difference Navier-Stokes solver. The algorithm uses explicit differencing with a choice of schemes including standard 4th order and 6th order schemes, and the Tam and Webb [9] 7-point stencil DRP scheme. Summation-by-parts boundary schemes are used for the differencing and fil-

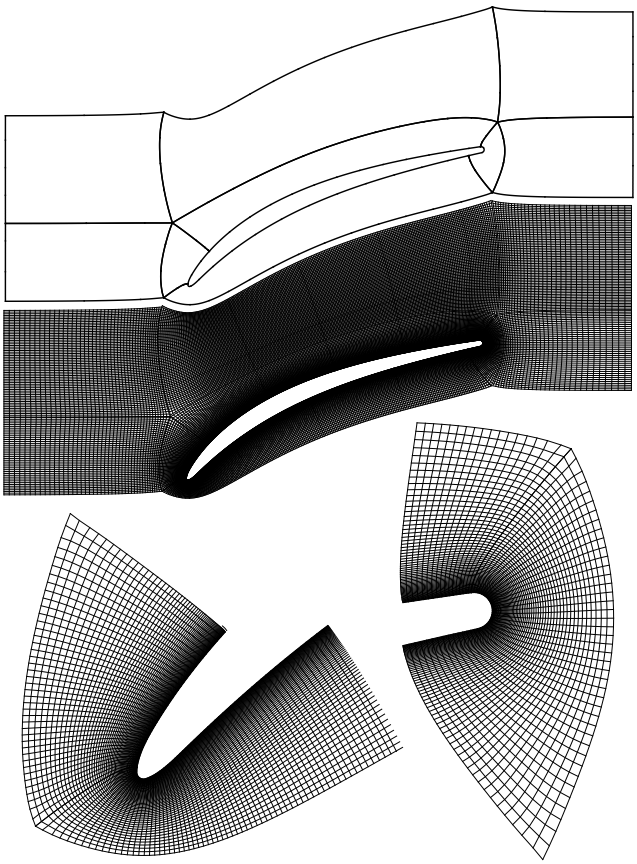

FIGURE 4. Block structure (upper) and example mesh (lower) showing every 4^{th} grid line with leading-edge and trailing-edge detail also showing every 4^{th} grid line ('datum' mesh)

tering schemes. The code solves the flow on structured grids which are curvilinear in the blade-to-blade plane, and uniform in the spanwise direction. Time integration is performed using a standard low-storage 4-step Runge-Kutta scheme. The code is multi-block and parallelization is achieved within each block. Characteristic boundary-conditions are applied at both exit and inlet; the method of Poinsot and Lele [10] is implemented. For the case where inflow turbulence is prescribed, the rates of change of velocity are imposed by imposing these on the characteristic variables.

The accuracy of the code has been verified by comparing results for the Taylor-Green Vortex case described by de Bonis [11], as shown in Figure 2. For this investigation the Tam and Webb scheme was used in combination with a standard 8th order filter. Figure 2 shows that this scheme has a comparable accuracy to a standard 8th order scheme.

Strong scaling performance of the code is shown in Figure 3; this shows a linear speed-up in the compute time per point for a $63M$ point multi-block mesh up to 1000 cores, which is the maximum number of cores used per case for the current investigation.

A description of the test-cases is given in Table 1. These will be described in more detail later. The focus of this work will be to simulate the stator passage flow at mid-span of the SMURF multi-stage compressor rig (described later). A description of the

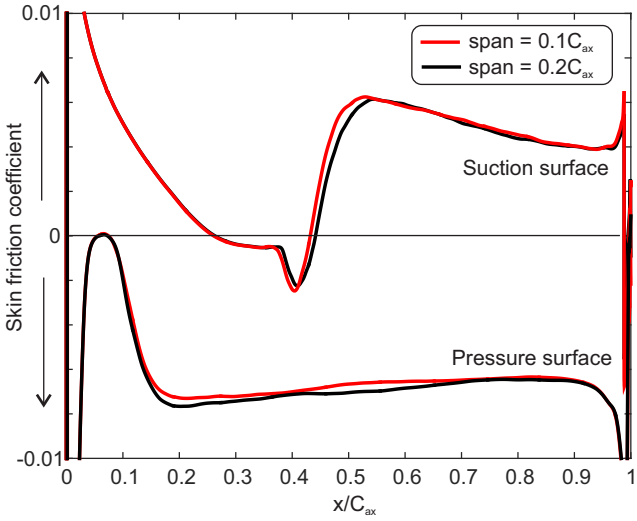

FIGURE 5. The effect of spanwise extent on predicted wall shear stress (cases *RE1E5*, *RE1E5W*)

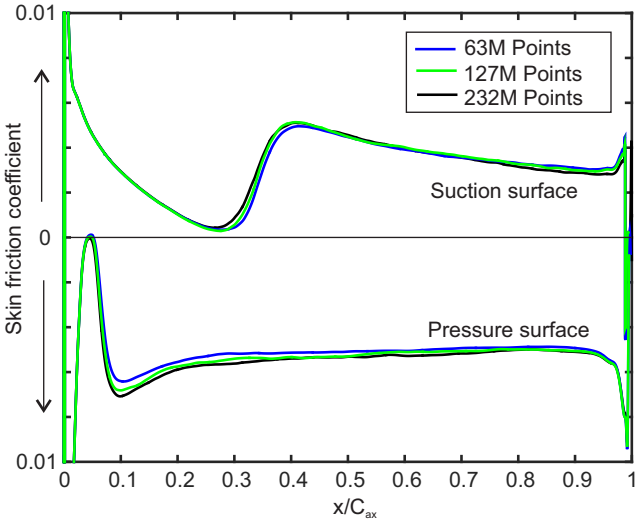

FIGURE 6. Comparison of predicted wall shear stress for three mesh sizes (cases *RE3E5*, *RE3E5F* and *RE3E5F2*)

test-cases used for mesh sensitivity checks is given in Table 2 and these are discussed in the following section.

Computational domain and mesh

The computational domain and example mesh showing the multi-block structure are shown in Figure 4. The geometry is taken from a midspan stator profile (discussed later) and extruded in the spanwise direction to generate a three dimensional domain. A spanwise domain height of 10% of axial chord was used throughout this study and periodicity was enforced in the spanwise direction. The effect of spanwise extent was tested by performing an additional testcase with a span of 20% of axial chord at $Re = 110k$; the results showed only small differences in the skin friction in the region of suction-surface transition (see Figure 5). Meshes were created using a combination of different software. Initially a coarse grid was created using the Turbo-

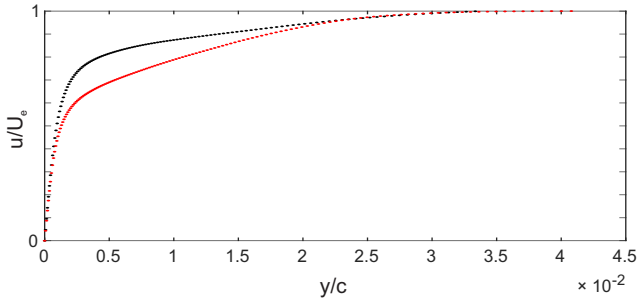

FIGURE 7. Example boundary-layer profiles ($x/C_{ax} = 0.75$) on the pressure (black) and suction (red) surfaces, 'datum' mesh $Re = 340k$, $Tu = 3.5\%$.

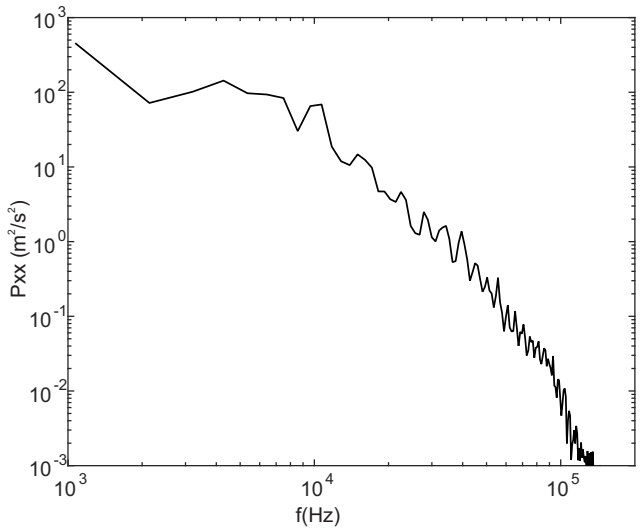

FIGURE 8. Example spectrum within the suction-side boundary-layer ($x/C_{ax} = 0.98$ and height within boundary layer $y^+ = 30$). 'Datum' mesh $Re = 340k$, $Tu = 3.5\%$.

TABLE 2. Mesh sensitivity test cases and near wall mesh spacing ($Re = 340k$ $Tu = 3.5\%$)

Test-case label	Mesh (no. points)	Δ_n^+	Δ_t^+	Δ_z^+
Re3E5	Datum (63M)	1.0	18	10.5
Re3E5F	Fine (127M)	1.0	14.9	8.8
Re3E5F2	Fine2 (240M)	1.0	12.5	7.3

grid software from ANSYS. This provided the block structure and block boundaries. A series of codes written in Matlab were then used to construct a much finer grid, ensuring optimum load balancing and near wall mesh control. The majority of the results described in this paper were obtained using a mesh with 63 million points (490k points in the blade-to-blade plane and 128 spanwise points); this will be referred to as the 'datum' mesh. Two finer meshes were also used and referred to as 'fine' and 'fine2'. These had around 25% and 50% more cells in each grid direction compared to the datum mesh, giving meshes of $127M$ and $240M$ points respectively. The mesh details and near-wall cell sizes are shown in Table 2. The near-wall cell sizes, particularly for the finer meshes, is similar to previous DNS studies such as [12], and so we will refer to the simulations as implicit LES/DNS throughout.

Cell sizes were compared to the Kolmogorov length-scale determined from the computed dissipation; cell sizes for the datum mesh were typically within 5 Kolmogorov length-scales. Previous DNS work (such as [13]) shows that the smallest scales in the flow are typically of the order of 10 Kolmogorov scales and grid independence is achieved when cell sizes are around 5-10 Kolmogorov lengths. Mesh sensitivity was analyzed by comparing results from the *RE3E5* case which had $63M$ mesh points with the results for the two finer grids (*RE3E5F* and *RE3E5F2*). The wall shear stress for these two cases is shown in Figure 6. The figure shows small differences around regions of transition on the suction and pressure surfaces, but in general the three cases are in very close agreement particularly on the suction-surface which is the main focus of this paper.

Figure 7 shows typical velocity profiles within the turbulent regions of the suction and pressure surfaces. The figure shows around 100 points within each boundary layer. Figure 8 shows an example of the power spectrum obtained in the aft suction surface for the 'datum' mesh, showing that the turbulent kinetic energy is resolved over around $3-4$ orders of magnitude.

Time-averaging

Time-average and statistical quantities were gathered during the simulations by summing the instantaneous conserved quantities $(\rho, \rho u, \rho v, \rho w, E_t)$ and also momentum terms $(\rho u^2, \rho v^2, \rho w^2, \rho uv, \rho uw, \rho vw)$. Time-average primitive variables were determined from these; this is equivalent to a Favre-average for velocity terms. Convergence of the statistics was checked by comparing the computed loss over different averaging times, to ensure the data was statistically stationary; typically, time-averages were computed over a time equivalent to 3 passings of the flow through stator passage.

Inflow turbulence generation

The inflow turbulence generation makes use of the library generated by Phillips and Fyfe [14] which generates a Gaussian turbulence spectrum. Turbulence fluctuations were pre-computed and then introduced at the inflow boundary at run-time. A length-scale and intensity were chosen to match experimental data obtained in a multi-stage compressor test rig as discussed later. A snap-shot of the structure of the free-stream turbulence in the region of the stator leading-edge is shown in Figure 9 which shows iso-surfaces of Q-criterion, which identifies vortical structures in the flow. Figure 10 shows contours of spanwise vorticity for cases with zero free-stream turbulence ('clean') and with $Tu = 3.5\%$. For the 'clean' case, on both the pressure and suction surfaces, the flow breaks down to turbulence via an essentially two-dimensional mechanism of Kelvin-Helmholtz roll-ups which eventually become three-dimensionally unstable. The addition of free-stream turbulence causes a much earlier breakdown to turbulence.

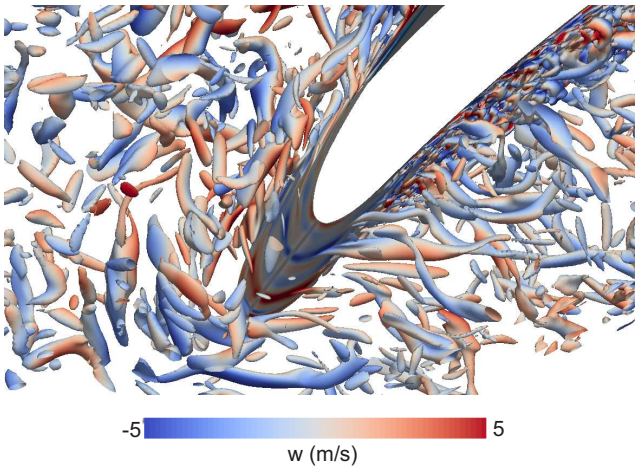

FIGURE 9. Iso-surfaces of Q-criterion $= 3 \times 10^7 s^{-2}$. Color indicates spanwise velocity

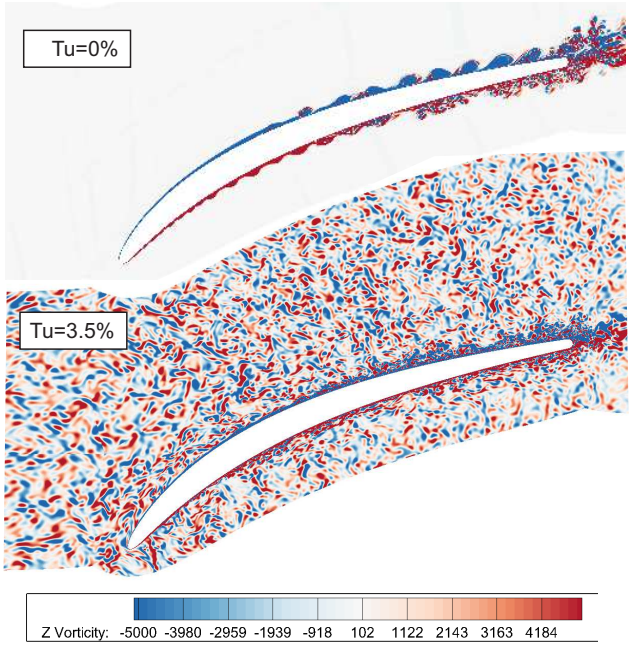

FIGURE 10. Instantaneous spanwise vorticity contours with and without freestream turbulence ($Re = 340k$)

Matching to rig conditions

The numerical study is undertaken on the mid-height profile of an embedded low speed compressor stage at the Whittle Laboratory. To ensure that the findings of the numerical study are representative of this stage, experimental measurements were compared with the results from the computational simulations. Firstly, the turbulence level and spectrum at mid-height stator inlet was measured and was used to verify that the inflow turbulence used in the simulations was representative. Secondly, to ensure that the loss was accurately predicted, the wake profile was measured and compared against the results of the simulations.

The SMURF Rig (see Figure 11) simulates a multi-stage high-pressure compressor; the rig is a 3-stage large-scale (1.5m

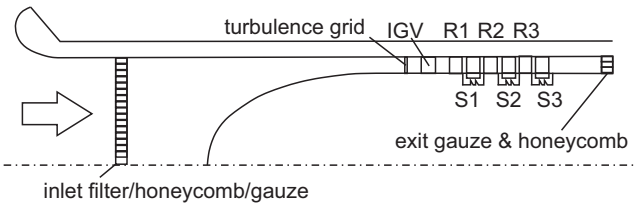

FIGURE 11. Schematic of the SMURF 3-stage compressor rig. R1, R2, R3 represent Rotor 1, 2 and 3, and S1, S2, S3 represent Stator 1, 2 and 3

diameter) model, which operates at low Mach number ($M \approx 0.1$) with cylindrical and parallel endwalls. The simulations were performed to match the stator 3 (S3) design-point conditions; the Reynolds number based on stator inlet conditions and chord is $Re = 340k$ and the inlet flow angle is 46^o. At these conditions the flow at mid-span of the stator is very closely two-dimensional; changes in midspan streamtube height from stator inlet to exit were measured to be around 3%. The stator geometry at midspan was also essentially two-dimensional, and as such the simulations were run with both 2-dimensional geometry and boundary conditions. In order to ensure the inflow turbulence simulated in the simulations was representative of the rig conditions, a length-scale and intensity were chosen to match experimental data obtained from hotwire measurements at the inlet to the stator within the multi-stage compressor test rig, which in this case were 1% of chord and $Tu = 3.5\%$ respectively. A comparison of the measured turbulence spectrum and the spectrum from the simulations is shown in Figure 12; the spectrum is taken at a plane downstream of the inlet plane and $0.25C_{ax}$ upstream of the stator leading-edge. The peaks in the measured spectrum are due to the blade-passing and harmonics and are therefore not captured in the simulations. In terms of the non-rotor-resolved unsteadiness, the results show that the prescribed spectrum matches closely the experimental measurement and thus the simulated turbulence represents reasonably well the multi-stage environment albeit in the absence of wakes.

A comparison of the total-pressure wake profile measured at Stator 3 exit and the prediction (case *Re3E5*) is shown in Figure 13. In the free-stream the experimental data shows the redistribution of total pressure across the passage due to the effects of upstream wakes. Since there are no rotor wakes in the computational simulations, the total pressure outside of the wakes is relatively uniform. Within the wake both the computational and experimental data match closely, both in terms of the wake depth and width; the computed wake depth and width are around 1.5% shallower and 3.5% wider than the experiment respectively. Although rotor wakes are not included in the simulation, this comparison indicates that the loss and mixing of the wake from the simulation to a large extent captures that observed in a representative multi-stage environment, despite the absence of wakes.

Figure 14 shows the instantaneous shear stress on the suction and pressure surfaces at the four Reynolds numbers tested. Over this range of Reynolds numbers, the transition process on the suction side changes from separated flow transition for $Re = 110k$ and $220k$ to attached-flow transition at $Re = 408k$. For $Re = 340k$, the suction surface was observed to experience

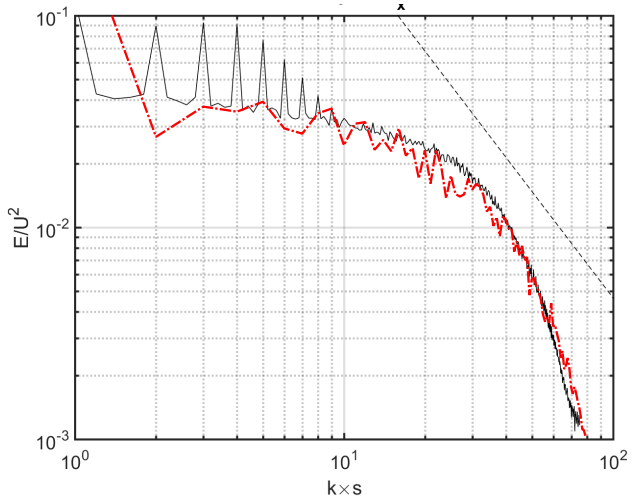

FIGURE 12. Comparison of the predicted turbulence spectrum (red) at 25% axial chord upstream of the stator leading-edge, and measured spectrum in the multi-stage rig at midspan Rotor 3 exit (black)

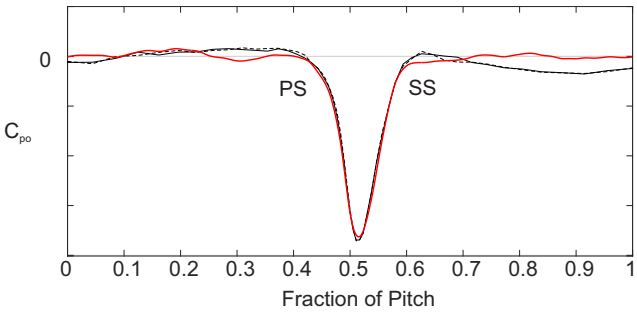

FIGURE 13. Comparison of predicted total pressure wake profile (red) with experimental measurement measured in the multi-stage rig (black)

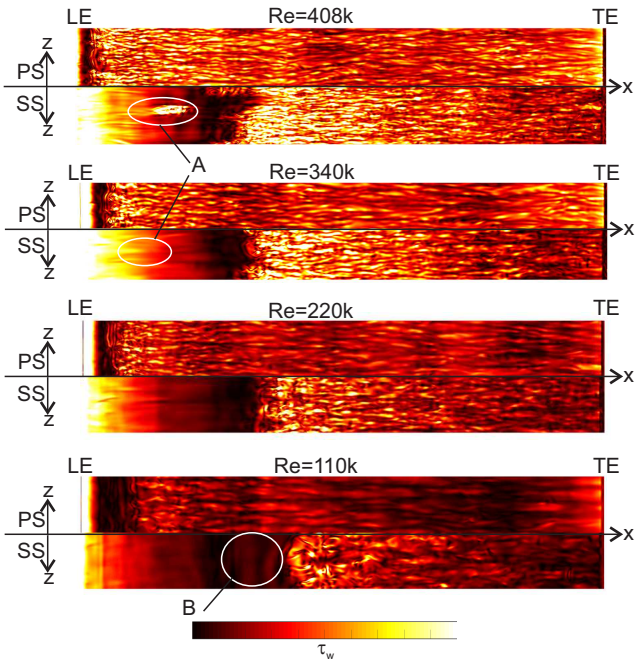

FIGURE 14. Instantaneous wall shear stress on the suction surface (SS) and pressure surface (PS)

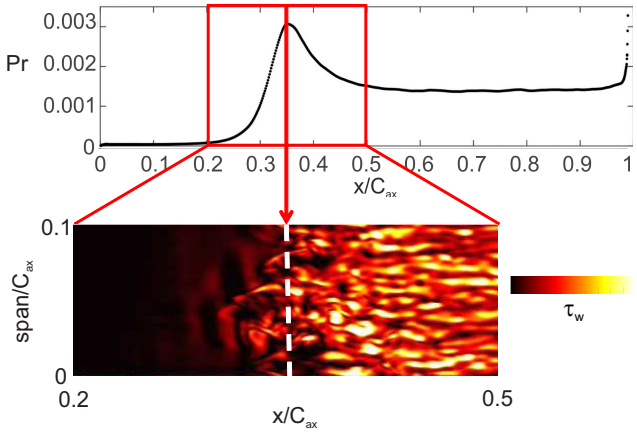

FIGURE 15. Suction surface turbulence production (top) and instantaneous wall shear stress ($Re = 340k$, $Tu = 3.5\%$)

intermittently attached and separated flow transition and therefore represents a case on the boundary between separated and attached flow transition.

The growth of instabilities in the boundary layer are also shown Figure 14. Klebanoff streaks (labelled A) can be observed upstream of the transition point. The intensity of these streaks appears to reduce as the Reynolds number is reduced. Streaks are also observed downstream of the transition regions on both pressure and suction surfaces, although again the intensity of these streaks reduces with Reynolds number. Reducing Reynolds number also gives rise to separated-flow transition and the emergence of two-dimensional Kelvin-Helmholtz roll-ups (labelled B).

QUESTION 1: HOW LARGE IS THE NON-EQUILIBRIUM REGION?

The simulations can be used to calculate the percentage of the suction surface boundary layer which exhibits non-equilibrium behaviour. This is achieved by determining the integrated turbulence production across the boundary layer Pr according to Equation 2:

$$Pr = -\frac{1}{U_e{}^3}\int_0^{\delta} \overline{u_i u_j}\frac{\partial U_i}{\partial x_j} dy. \qquad (2)$$

In order to illustrate how the region of non-equilibrium is determined, Figure 15 shows the variation of suction surface Pr with axial distance for $Re = 340k$ and a snapshot of the instantaneous wall shear stress in the region of peak turbulence production. We choose the start of the turbulent non-equilibrium region as the point of peak Pr; since the focus of this paper is on the turbulent non-equilibrium region we do not include the region of transition upstream of this point in the estimation of non-equilibrium length. Turbulence production correlates closely with intermittency but was found to be a more robust method to determine the end point of transition for the cases considered here. Downstream of the point of peak Pr, the flow is essentially fully turbulent and there is no indication of intermittent laminar

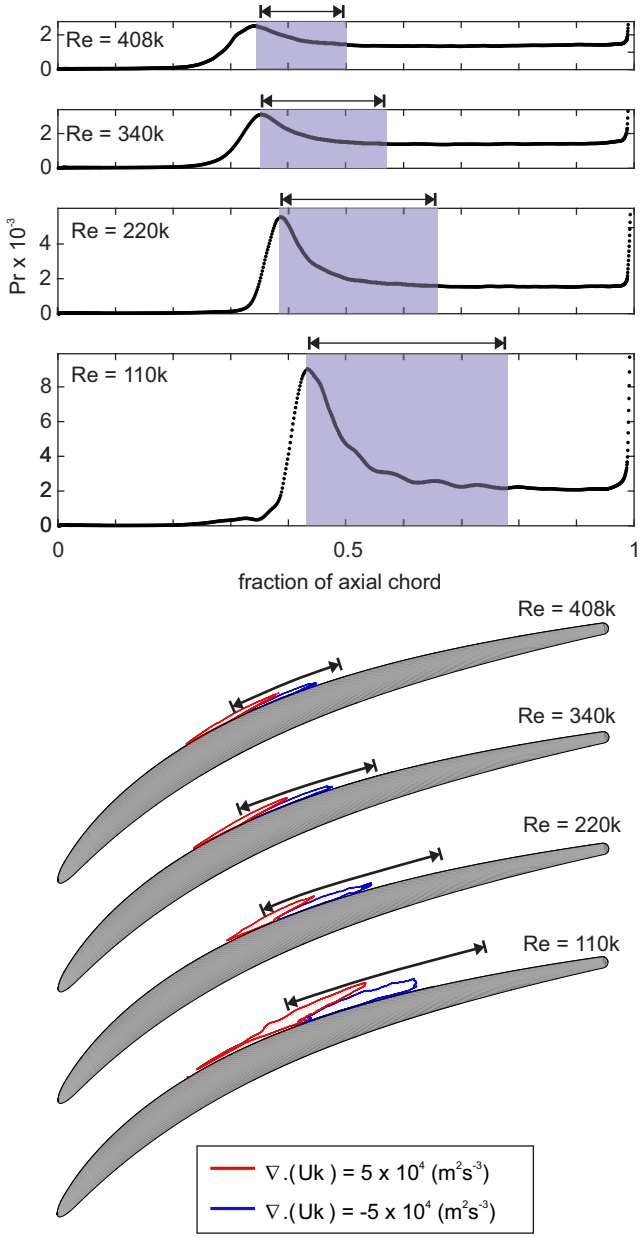

FIGURE 16. Turbulent kinetic energy production and divergence of turbulent kinetic energy flux in the region of suction-surface transition.

regions which are observed in the wall shear stress upstream of the peak production point. The end point of the non-equilibrium region is determined as the point where Pr is within 2% of the far downstream value (in this case at $90\%C_{ax}$).

The lengths of the non-equilibrium regions for the cases tested here are shown in Figure 16. The turbulence production for all the Reynolds numbers tested is shown in the top of the figure and the non-equilibrium region determined by the method described above is indicated on the plots by the shaded regions. The lower part of the figure will be discussed later. The figure shows that non-equilibrium regions affect a significant portion of the blade surface: around 15% of the suction surface at $Re = 408k$, increasing to 35% of the suction surface at $Re = 110k$. The non-equilibrium wetted area is of a similar size to the laminar wetted area, and in this case both reduce with Reynolds number by a similar proportion.

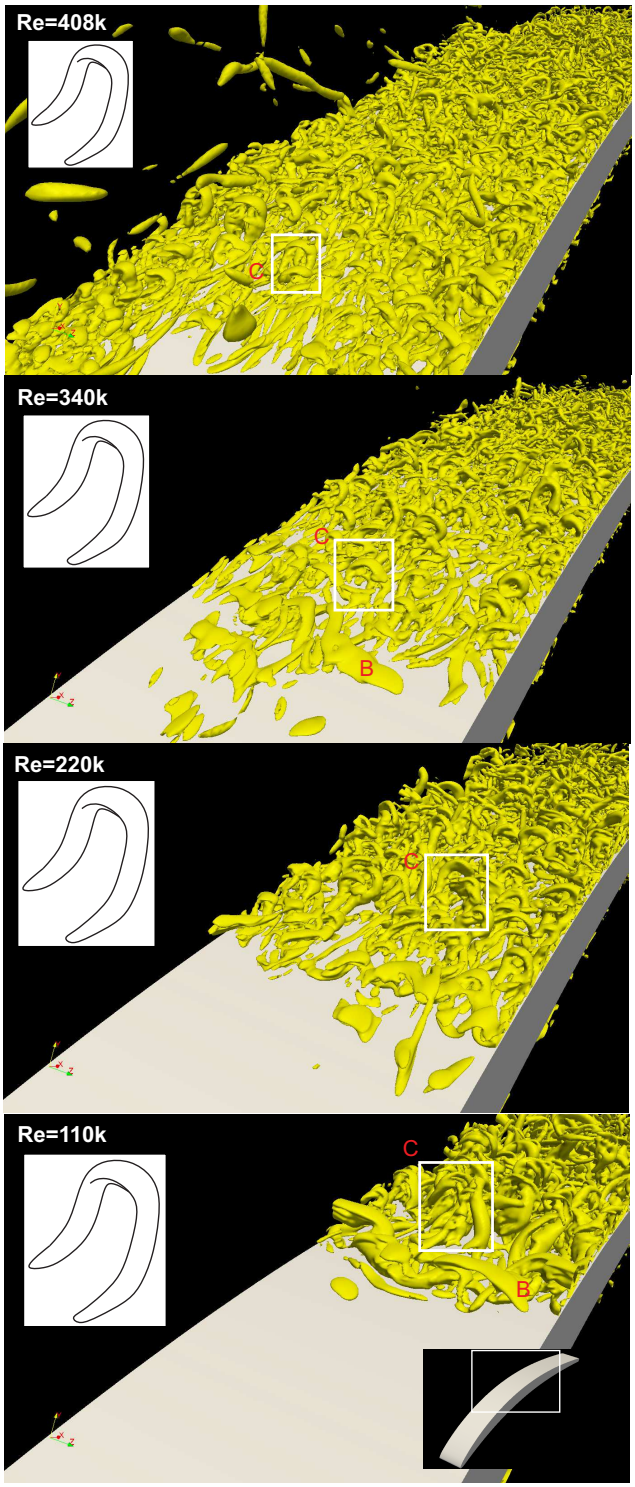

FIGURE 17. Suction-surface flow structure indicated by iso-surfaces of Q-criterion $= 3 \times 10^8 s^{-2}$. ($Tu = 3.5\%$)

QUESTION 2: WHAT IS THE MECHANISM RESPONSIBLE?

In this section we discuss the role of the flow structure on non-equilibrium behaviour. The unsteady flow structures on the

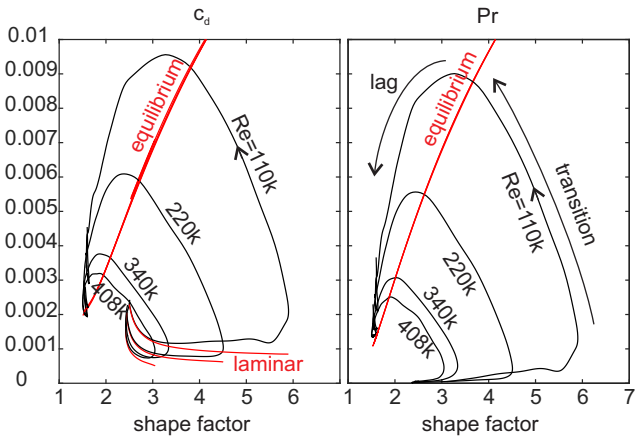

FIGURE 18. Variations of c_d and Pr with shape factor.

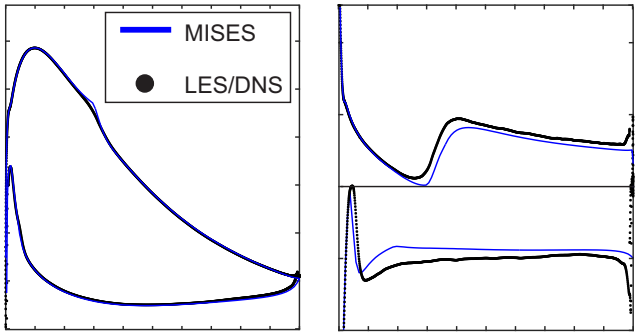

FIGURE 19. Loading and skin friction comparison with MISES with prescribed transition ($Re = 340k$)

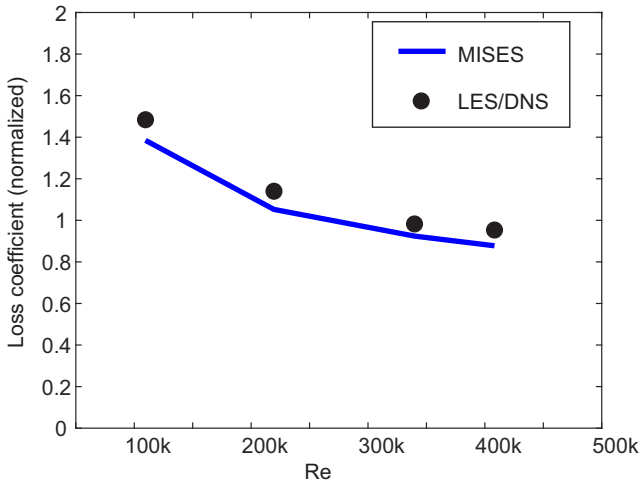

FIGURE 20. Loss prediction comparison with MISES with prescribed transition

suction-surface are observed in Figure 17. As discussed above, at low Reynolds numbers ($Re = 110k$ to $220k$) transition occurs through separation and shifts to attached flow transition at $Re = 408k$. The figure shows that in general both two-dimensional and three-dimensional instabilities occur within the transition region; spanwise roll-ups develop in the separated shear-layer (an example of which is labelled B), and these are followed by three-dimensional breakdown to turbulence. The development of two-dimensional instabilities clearly moves downstream as the Reynolds number is reduced. The three-dimensional breakdown to turbulence leads to the formation of hair-pin structures (labelled C) as widely reported in previous studies of turbulent boundary layers (see for instance [15,16]). These grow in size as the Reynolds number is reduced.

The lower part of Figure 16 shows the regions where the turbulence production and dissipation are out of balance. These regions are determined from the advection of turbulent kinetic energy $\vec{V}k$ assuming turbulent diffusion is small; contours indicating regions where the production rate either significantly exceeds the turbulent dissipation rate (i.e., $\nabla \cdot (\vec{V}k) >> 0$) are shown in red, and contours where the dissipation is significantly larger than the production rate ($\nabla \cdot (\vec{V}k) << 0$) are shown in blue. The figure shows that the dissipation lags significantly behind the production of turbulence. In the region of transition the production spreads from near the wall to the outer boundary-layer, while the dissipation growth lags the production and remains confined to the near-wall flow. Both these regions of imbalance increase in size as the Reynolds number is reduced. This is consistent with the increase in length of the non-equilibrium region observed above.

The length of the non-equilibrium region is determined, therefore, by the size of hair-pin type structures within the turbulent boundary layer since the time-scale over which these structures transfer energy to smaller scales will be determined by their length-scale. The structure sizes increase at lower Reynolds numbers, thereby increasing the length of the non-equilibrium region.

QUESTION 3: WHAT IS THE IMPACT ON LOSS?

The mechanical energy equation for an incompressible Reynolds-Averaged flow is:

$$\frac{DK}{Dt} = -\frac{1}{\rho}\frac{\partial}{\partial x_j}\left(pU_j + \overline{u_i u_j}U_i\right) + \nu\frac{\partial^2 K}{\partial x_j^2} + \overline{u_i u_j}\frac{\partial U_i}{\partial x_j} - \nu\left(\frac{\partial U_i}{\partial x_j}\right)^2 \quad (3)$$

The term on the left-hand-side of this equation is the transport of mean kinetic energy $K = 0.5U_i^2$. On the right-hand-side, the first two terms represent mechanical work on the boundaries and diffusion of mean kinetic energy; thus these terms represent a re-distribution of mechanical energy within the flow. The final two terms represent the destruction of mechanical energy due to turbulent shear work (i.e. turbulence production) and the shear work done by the mean strain. These latter two terms lead to the dissipation of mean kinetic energy and can be used to form a

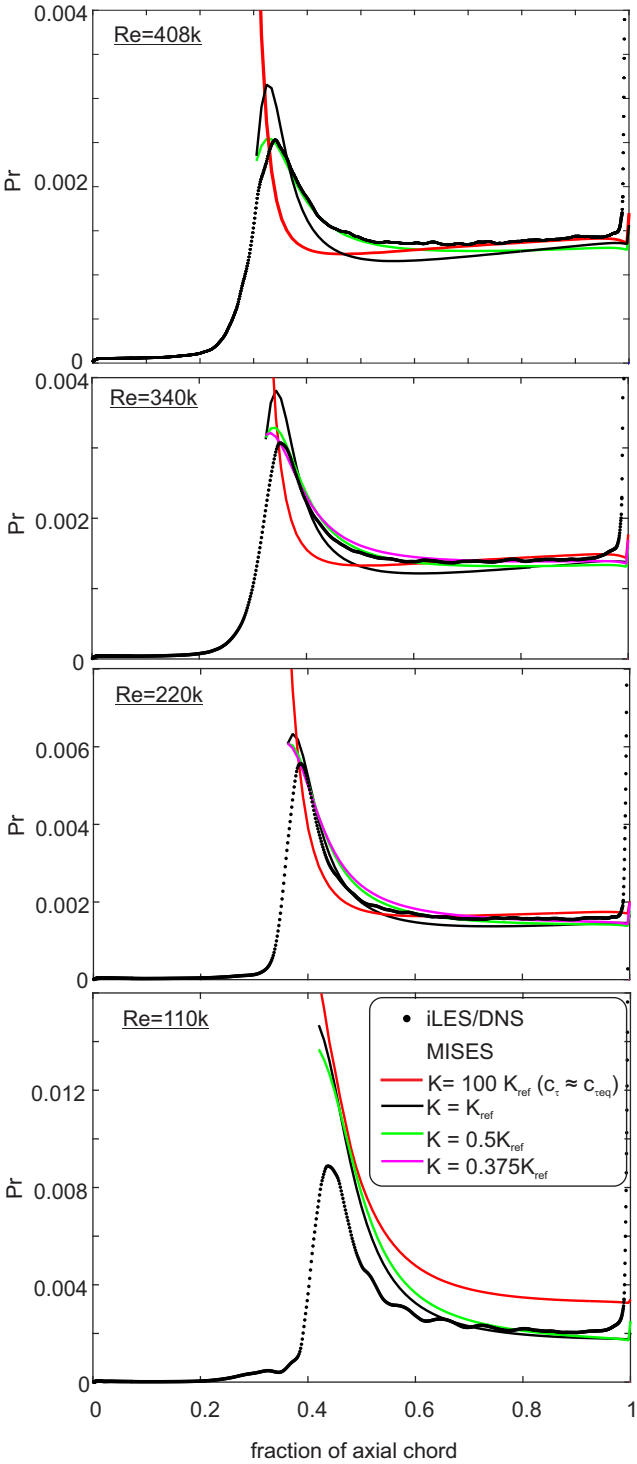

FIGURE 21. The effect of shear-lag constant K on turbulence production as compared to iLES/DNS.

dissipation coefficient for a Reynolds-Averaged boundary layer:

$$c_d = \frac{1}{{U_e}^3}\int_0^\delta \left(-\overline{u_i u_j}\frac{\partial U_i}{\partial x_j} + \nu\left(\frac{\partial U_i}{\partial x_j}\right)^2\right) dy = Pr + \frac{1}{{U_e}^3}\int_0^\delta \nu\left(\frac{\partial U_i}{\partial x_j}\right)^2 dy \quad (4)$$

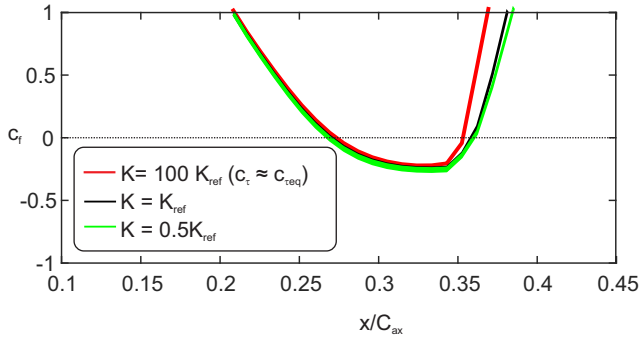

FIGURE 22. Skin friction in region of suction-surface separation bubble ($Re = 220k$).

It is important to note that here c_d represents the loss of mechanical energy of the mean flow rather than the loss of the total mechanical energy of the flow (which would also include the turbulent kinetic energy as well, as shown by Rotta [17]). This choice is consistent with the definition of dissipation coefficient used in the low-order modelling discussed later. This is also consistent with the dissipation coefficient which would be computed using conventional RANS CFD.

Figure 18 shows the variation in c_d and Pr with shape factor H determined from the simulations. The figure shows the rise in c_d and Pr as the boundary layer undergoes transition which in turn causes the shape factor to reduce as the flow develops towards the trailing-edge. Also shown are the variations in c_d and Pr estimated from correlations for equilibrium boundary layers using the local Re_θ and H taken from the simulations. The lines for equilibrium turbulent boundary-layers collapse onto one line for the cases tested here. The figure shows that over the range of shape factors which the boundary layer experiences downstream of transition ($H = 2-4$), the equilibrium c_d is a strong function of shape factor. It is interesting to note that the actual c_d passes through the equilibrium line close to the point of peak turbulence production. Thus, the rate at which the boundary layer reaches an equilibrium state determines the loss generation in the non-equilibrium region.

Low-order modelling

In order to determine how non-equilibrium turbulence affects loss a method which de-couples the effects of transition and non-equilibrium behaviour is required. Here we use an industry-standard reduced order model in order to do this. The reduced-order model commonly used in industry to predict profile loss is MISES [18]. MISES is a steady 2D/quasi-3D Euler code with a coupled boundary-layer solver. For the current work, 2D calculations were performed, where the boundary conditions were set to match the iLES/DNS simulations.

In the following sections we first compare the loss prediction from MISES with Reynolds number with the iLES/DNS data to verify that MISES gives the correct variation in loss with Reynolds number. Then we compare the turbulence production from MISES with the iLES/DNS to determine the veracity of the non-equilibrium model in MISES.

For the current investigation the suction surface and pres-

sure surface transition points are prescribed in MISES at a point to match the transition point observed in the iLES/DNS simulations. As explained above, this was estimated from the point of peak turbulence production *Pr* (see Figure 15). Comparisons of the predicted loading and skin-friction from MISES and the iLES/DNS are shown in Figure 19. The results show that this method of prescribing transition achieves a close match in both loading and skin friction.

A comparison of the loss variation with Reynolds number is shown in Figure 20. This figure shows that MISES tends to predict a loss around 5% lower than the high-fidelity simulations, while the variation in loss with Reynolds number is in close agreement with the iLES/DNS. The exit flow angle predicted by MISES (not shown here) was also in close agreement with the simulations, being within 0.03deg for all cases tested.

The results verify the ability for MISES to predict performance when transition is prescribed to match the high-fidelity simulations.

In the next section we verify the accuracy of the non-equilibrium model in MISES.

Validation of shear-lag model

The dissipation coefficient is determined in MISES by the skin friction coefficient c_f and the Reynolds stress coefficient $c_\tau = (\overline{u'v'}/u_e)_{max}$:

$$c_d = \frac{c_f}{2} U_s + c_\tau (1 - U_s), \tag{5}$$

where U_s is an effective normalized slip velocity determined from the local shape factor and momentum thickness Reynolds number Re_θ. The first term on the right hand side of the equation represents the dissipation due to the time-average strain within the boundary layer, while the second term on the right accounts for the conversion of kinetic energy from the base flow into turbulent kinetic energy; this is the shear work done by the turbulent stresses in the boundary layer.

The approach in MISES is to assume that the skin friction c_f responds immediately to the change in boundary layer state at transition, while the turbulent shear c_τ responds according to a shear-lag model determined by Equation 6:

$$\frac{\delta}{c_\tau}\frac{dc_\tau}{ds} = K\left(\sqrt{c_{\tau eq}} - \sqrt{c_\tau}\right), \tag{6}$$

where K is the lag constant. The actual c_τ lags the local equilibrium value $c_{\tau eq}$ which is derived from the $G-\beta$ turbulent equilibrium locus [7]. MISES only uses the shear-lag equation downstream of transition; upstream of transition laminar correlations are used to determine the dissipation and c_τ is not used. This is essentially a transport equation for turbulent shear. In order to solve Equation 6, the value for c_τ at transition is required, which MISES determines from the following correlation:

$$c_\tau = c_{\tau eq} \times 3.24 \exp\left(\frac{-6.6}{H-1}\right). \tag{7}$$

The accuracy of the shear-lag model can be assessed by comparing the MISES turbulence production term $Pr = c_\tau(1-U_s)$ with the turbulent production within the boundary layer predicted by the high fidelity simulations (see Equation 2)

The turbulent production from the iLES/DNS and the reduced order model are shown in Figure 21. The reduced order model has been run with four values of lag constant K. These are the reference value used by default in MISES $K = K_{ref} = 5.6$, and values $K = 0.5K_{ref}, 0.375K_{ref}$ and $K = 100K_{ref}$. Cases where $K = 0.5K_{ref}$ and $0.375K_{ref}$ are cases where equilibrium behaviour is delayed. $K = 100K_{ref}$ ensures near equilibrium behaviour. For this case, Equation 7 was modified so that the transition point value of c_τ was set to the equilibrium value. It should be noted that because the boundary layer development is modified by changes in the shear lag, this also modifies $c_{\tau eq}$, and therefore downstream of the transition point the values of $c_{\tau eq}$ in the 'equilibrium' case depart from the $c_{\tau eq}$ values for the other non-equilibrium cases.

For the three highest Reynolds numbers ($Re = 220k$, $340k$ and $408k$) the shear-lag model is observed to accurately predict the non-equilibrium behaviour (see Figure 21). The values of K which give the closest agreement with the high fidelity simulations are $K = 0.5K_{ref}$ and $0.375K_{ref}$. For the lowest Reynolds ($Re = 110k$) the shear-lag model was found to substantially overestimate the initial turbulence production after transition. At $Re = 110k$ it was not possible to obtain data when $K = 0.375K_{ref}$ due to the development of large separations which gave rise to poor convergence. In this Reynolds number regime bubble sizes become large and this shear-lag model is unlikely to perform well in this case. It is interesting to note that despite its simplicity, this shear-lag model performs remarkably well in terms of capturing the correct turbulence production.

The results show that as K is reduced, and therefore non-equilibrium effects are increased, there is a reduction in the peak turbulence production this is important because this reduces the subsequent dissipation and therefore loss (as discussed later). The reduction in turbulence production was also found to affect the size of separation bubbles. Figure 22 shows the skin friction in the region of separation for $Re = 220k$. The figure shows that as the lag constant is reduced, the point of reattachment shifts downstream and the bubble length increases. The skin friction downstream of the bubble is also modified. The reduction in turbulence production as K is reduced delays reattachment meaning that a thicker boundary layer is generated further downstream when reattachment does eventually occur.

Effect of shear-lag constant on loss

The results so far indicate that non-equilibrium boundary layer behaviour can affect profile loss in two ways. First, non-equilibrium behaviour of attached turbulent boundary layers can lower profile loss by locally reducing the dissipation coefficient of the boundary layer. Secondly, non-equilibrium behaviour of separated boundary layers can delay reattachment and thus increase the bubble size thus increasing loss. In this section we make use of the reduced-order model to determine the effect of non-equilibrium boundary layers on loss as suction surface transition position is varied.

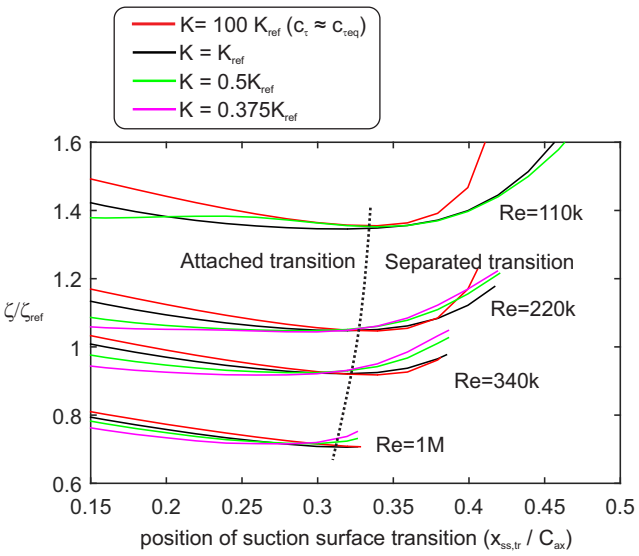

FIGURE 23. The effect of transition point and lag-constant K on suction surface boundary layer loss as predicted by MISES.

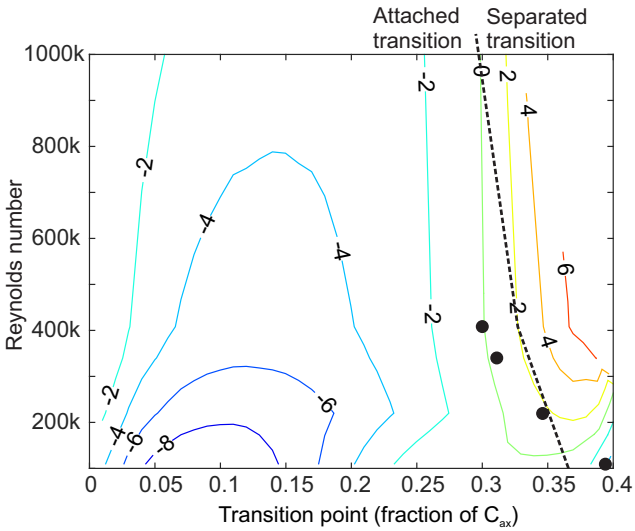

FIGURE 24. Predicted percentage change in suction-surface loss due to non-equilibrium boundary layers. iLES/DNS data indicated by the black dots.

Figure 23 shows the variation of loss at a range of Reynolds numbers $Re = 110k - 1M$ using MISES with prescribed transition points from close to the leading-edge (where the flow is attached) to further downstream to where separation occurs (as indicated on the figure). For each Reynolds number line, the loss has been determined at a range of prescribed transition points and shear-lag constants. Results are shown for a range of lag constants, to indicate how non-equilibrium effects modify the loss. As above, data for $K = 100K_{ref}$ indicates the loss for an equilibrium boundary layer. The figure shows that in general non-equilibrium effects tend to reduce loss a part from in regions of separated flow transition.

Figure 24 shows contours of the percentage change in loss between equilibrium cases $K = 100K_{ref}$ and cases with $K = 0.375K_{ref}$ to indicate the potential effect of non-equilibrium boundary layers on loss. The figure shows that in regions of attached flow, non-equilibrium effects reduce loss by as much as 8%. The benefit results directly from the lower suction surface loss because non-equilibrium effects reduce turbulent shear (production) within the boundary layer. As transition moves downstream, and the flow moves from attached to separated flow this behaviour reverses and equilibrium effects increase loss by up to 6%. The delay in turbulence production now tends to increase loss; in this case the delay in production leads to a delay in the bubble closure and thus higher bubble losses as shown earlier. Therefore, over a wide range of flow conditions (from attached to separated flow transition) the overall variation in loss which could occur due to non-equilibrium effects is 14%.

In order to indicate where a real compressor blade might operate, shown in Figure 24 is the variation in transition location determined from the iLES/DNS data. As Reynolds number is increased from $Re = 110k$ to $408k$ the compressor blade moves from separated flow transition to attached flow transition and thus from a region where non-equilibrium tends to increase loss to a region where non-equilibrium reduces loss. Whether this benefit can be exploited remains to be determined.

CONCLUSIONS

The paper addressed three questions. The first of these was to determine the extent to which non-equilibrium turbulence affects compressor boundary layers. The results show that for the Reynolds numbers tested in the paper ($Re = 110 - 408k$), non-equilibrium turbulent boundary layers affected between $15 - 35\%$ of the suction surface, which was comparable to the regions of laminar wetted area for a given Reynolds number.

The second question was to determine the mechanism driving the size of the non-equilibrium region. The predominant structures within the turbulent boundary layer were hair-pin type structures, whose size scaled inversely with Reynolds number. The lag between turbulence production and dissipation scaled with the size of the hairpin structures and thus as Reynolds numbers were reduced the amount of non-equilibrium flow increased. This behaviour was broadly captured by a shear-lag model. We found that if the model constant was tuned to match the iLES/DNS, the shear-lag model used in MISES did broadly predict the correct turbulence production, albeit with a value of lag constant around half of the current recommended value.

Finally, using this model we then determined the effects on loss of non-equilibrium turbulence. The results indicated two non-equilibrium effects on loss. For all cases, non-equilibrium behaviour tends to reduce peak turbulence production which reduces loss for attached flow cases by as much as 8%. If transition occurs through separation an additional effect of non-equilibrium is to delay reattachment, which tends to increase loss by up to 6%. The overall variation in loss which could occur due to non-equilibrium effects is 14% moving from attached to separated flow transition.

This raises the question of whether it is possible to exploit non-equilibrium effects to reduce loss. Whether this may be achievable (for instance through different loading distributions, surface roughness or by exploiting the effect of incoming wakes) remains to be determined.

ACKNOWLEDGMENT

Development of the 3*DNS* code used for this work has been undertaken as part of EPSRC project $EP/L027437/1$. The authors also gratefully acknowledge the support of Rolls-Royce plc who funded the computational costs for this work, and Pawel J. Przytarski who provided the data given in Figure 2.

NOMENCLATURE

c	chord
C_{ax}	Axial chord
c_d	Dissipation coefficient
c_f	Skin friction coefficient
C_p	Pressure coefficient
C_{po}	Total pressure coefficient
c_τ	Reynolds stress coefficient
H	Shape factor
k	Turbulent kinetic energy
M	Mach number
p	Pressure
Pr	Turbulence production rate
$p_\circ$	Stagnation pressure
Re	Reynolds number based on inlet conditions and chord
s	Entropy, surface distance
$\dot{S}_a$	Entropy generation rate per unit surface area
T	Temperature
T_s	Isentropic temperature
$T_\circ$	Stagnation temperature
Tu	Turbulence intensity
t	Time
U_e	Boundary layer edge velocity
$\vec{V}$	Velocity vector
V_{in}	Inlet velocity
x	Axial distance

GREEK LETTERS

α	Flow angle
δ	Boundary layer thickness
δ^*	Displacement thickness
δ_e	Energy thickness
θ	Momentum thickness
ρ	Density
ζ	Loss coefficient

REFERENCES

[1] Cumpsty, N. A., 1989. *Compressor Aerodynamics*. Longman Scientific & Technical.

[2] Denton, J. D., 1993. "Loss mechanisms in turbomachines". *ASME J. Turbomach.,* **115**, pp. 621–656.

[3] Mayle, R. E., 1991. "The role of laminar-turbulent transition in gas turbine engines". *ASME J. Turbomach.,* **113**, pp. 509–537.

[4] Walker, G. J., 1993. "The role of laminar-turbulent transition in gas turbine engines a discussion". *ASME J. Turbomach.,* **115**, pp. 207–218.

[5] Schreiber, H. A., Steinert, W., and Kusters, B., 2002. "Effects of reynolds number and free-stream turbulence on boundary-layer transition in a compressor cascade". *ASME J. Turbomach.,* **124**, pp. 1–9.

[6] Hughes, J. D., and Walker, G. J., 2001. "Natural transition phenomena on an axial compressor blade". *ASME J. Turbomach.,* **123**, pp. 392–401.

[7] Green, J., Weeks, D., and Brooman, J., 1977. "Prediction of turbulent boundary layers and wakes in compressible flow by a lag-entrainment method". *R M Report 3791,Aeronautical Research Council, HMSO, London*.

[8] Drela, M., 2014. *Flight Vehicle Aerodynamics*. MIT Press.

[9] Tam, C. K. W., and Webb, J. C., 1993. "Dispersion-relation-preserving finite difference schemes for computational acoustics". *Journal of Computational Physics,* **107**, pp. 262–281.

[10] Poinsot, T. J., and Lele, S. K., 1992. "Boundary conditions for direct simulations of compressible viscous flows". *Journal of Computational Physics,* **101**, pp. 104–129.

[11] DeBonis, J., 2013. "Solutions of the Taylor-Green Vortex Problem Using High-Resolution Explicit Finite Difference Methods". *51st AIAA Aerospace Sciences Meeting including the New Horizons Forum and Aerospace Exposition*(February).

[12] Zaki, T. A., Wissink, J. G., Rodi, W., and Durbin, P. A., 2010. "Direct numerical simulations of transition in a compressor cascade: the influence of free-stream turbulence". *Journal of Fluid Mechanics,* **665**, pp. 57–98.

[13] Yao, Y., Thomas, T., and Sandham, N. D., 2001. "Direct numerical simulation of turbulent flow over a rectangular trailingedge". *Theoretical and Computational Fluid Dynamics*, pp. 337–358.

[14] Phillips, L., and Fyfe, D., 2011. "Turbid: A routine for generating random turbulent inflow data". *Naval Research Laboratory Report,* **NRL/MR/6040–11-9357**.

[15] Robinson, S. K., 1991. "Coherent motions in the turbulent boundary layer". *Annual Review of Fluid Mechanics,* **23**.

[16] Adrian, R. J., 2007. "Hairpin vortex organization in wall turbulence". *Physics of Fluids,* **19**.

[17] Schlichting, H., 1968. *Boundary-layer theory*. McGraw-Hill Inc.

[18] Drela, M., and Youngren, H. *A user's guide to MISES 2.56*. MIT.